Available online at www.sciencedirect.com
ScienceDirect
Journal of the European Ceramic Society 26 (2006) 3181–3190
www.elsevier.com/locate/jeurceramsoc

Crystallography, microstructure and morphology of $Mg_4Nb_2O_9$/MgO and $Mg_4Ta_2O_9$/MgO interfaces formed by topotaxial solid state reactions

D.C. Sun [1], S. Senz, D. Hesse *

Max Planck Institute of Microstructure Physics, Weinberg 2, D-06120 Halle, Germany

Received 7 July 2005; received in revised form 6 October 2005; accepted 17 October 2005
Available online 27 December 2005

Abstract

$Mg_4Nb_2O_9$/MgO and $Mg_4Ta_2O_9$/MgO interfaces of definite crystallography were formed by topotaxial thin film solid state reactions in the systems MgO–Nb_2O_5 and MgO–Ta_2O_5. MgO (0 0 1) single crystal substrates, heated to different temperatures, were subjected to Nb–O and Ta–O vapors generated by e-beam evaporation in high vacuum. Thin films mainly containing the phases $Mg_4Nb_2O_9$ and $MgNb_2O_6$, respectively $Mg_4Ta_2O_9$ and $MgTa_2O_6$, were formed by gas–solid reactions. The crystallographic relationships between the product phases and the MgO substrate were systematically studied by X-ray diffractometry and transmission electron microscopy (TEM). Surprisingly pole figure analysis revealed more than one orientation relationship for some of the phases: $Mg_4Nb_2O_9$ and $Mg_4Ta_2O_9$ grew with (1 1 .4), (1 1 .6) and (1 1 .9) orientations, depending on temperature. Selected area diffraction patterns and high resolution TEM images show that these three orientations have a common $Mg_4(Nb/Ta)_2O_9$ [1 $\bar{1}$ .0]/MgO [1 $\bar{1}$ 0] axis and differ by the angle between the $Mg_4(Nb/Ta)_2O_9$ (0 0 .1) and MgO (1 1 1) planes. Crystallographic illustrations of this phenomenon are given, and possible origins and consequences for the solid state reaction are discussed. Indications for two different interfacial reaction mechanisms are found.

Keywords: Interfaces; Defects; Electron microscopy; Niobates; Tantalates

1. Introduction

Solid state reactions in oxide ceramics are being widely studied due to their importance for both fundamental condensed matter research and practical use.[1–3] AB_2O_4 spinel-forming reactions, in which a binary oxide AO of rock-salt structure reacts with another binary oxide B_2O_3 of, e.g., corundum structure to form a spinel, are among the most interesting model systems for solid state reactions that lead to ternary or quaterny oxides as product phases.[1,4–6] Topotaxial reactions involving a certain orientation relationship between the initial and product phases are particularly useful, if reaction mechanisms are to be studied. In many cases the latter can be deduced from the atomic-scale structure of the reaction front.[4,15]

Previously, some of us studied a series of topotaxial reactions with MgO (0 0 1) single crystals,[5,6] forming $MgAl_2O_4$ (−4.1% lattice misfit with MgO), $MgCr_2O_4$ (−1.1%), $MgFe_2O_4$ (−0.4%), Mg_2TiO_4 (+0.17%), Mg_2SnO_4 (+2.5%), and $MgIn_2O_4$ (+4.5%) spinels with different values of spinel/MgO lattice misfit (given in parentheses). In such cases of cube-on-cube orientation, the structure of the reaction fronts and the mechanism of the interfacial reaction were determined by the sign and amount of the lattice misfit.[4,15] At positive misfit, the Burgers vector of the misfit dislocations present at the reaction front points out of the interface, enabling the dislocation to glide, when coping with the movement of the advancing reaction front. At negative misfit, the Burgers vector lies in the interface plane, so that a climb process is required for the movement of the dislocations. (At very low misfit, e.g., 0.17%, no interfacial dislocations form and the misfit is accommodated by point defects.) In the present work, these studies are extended to two systems of higher complexity, viz. Nb_2O_5–MgO[7,8] and Ta_2O_5–MgO,[9,10] which involve more than one product phase, none of which has a cubic lattice.

Some of the formed phases have a technical significance. $Mg_4Nb_2O_9$ is known to exhibit luminescence in the blue–green region and it is studied as a potential candidate material for high-definition television (HDTV) and projection TV applications.[11]

* Corresponding author. Tel.: +49 345 5582 741; fax: +49 345 5511 223.
E-mail address: hesse@mpi-halle.de (D. Hesse).
[1] Present address: Beijing International Technology Cooperation Center, Wangjing Zhonghuan, Nanlu 9, Chaoyang District, Beijing 100102, PR China.

0955-2219/$ – see front matter © 2005 Elsevier Ltd. All rights reserved.
doi:10.1016/j.jeurceramsoc.2005.10.007

In the scope of candidates for nonlinear-optical and laser materials, Bruck et al.[12] reported the growth and optical properties of compounds in the $MgO–Nb_2O_5$ binary system. Generally, interfaces in ceramic composite materials play an important role in many technologically relevant composite materials.[13] The mechanical properties of such materials are, to a large extent, controlled by the microstructure of the interfaces.[14] Detailed knowledge of the microstructure of these interfaces is helpful for tailoring the properties of composite materials for advanced applications. High resolution transmission electron microscopy (HRTEM) is particularly suited to obtain information about the atomic structure of interfaces.

In this work, TEM and HRTEM are employed in addition to XRD, to study the microstructure of reaction fronts forming during topotaxial reactions in non-cubic systems.

2. Experimental

In the reaction experiments, polished (0 0 1) surfaces of MgO single crystals 10 mm × 10 mm × 1 mm in size (from CrysTec GmbH, Berlin, Germany) were subjected to either Nb–O or Ta–O vapor, respectively. The vapors were produced by electron-beam evaporation of either an Nb_2O_5 or Ta_2O_5 target in a high-vacuum system. The targets were made of Nb_2O_5 or Ta_2O_5 powder of 99.9985% purity (from Johnson Matthey GmbH) by cold pressing under 35 kN and sintering at 1200 °C for 1 h. Prior to the reaction experiments the MgO substrates were heated in air at 1200 °C for 1 h.

The base pressure of the vacuum system was 1×10^{-3} Pa. During deposition, 99.999% pure oxygen was introduced to establish a pressure of 1.0×10^{-2} Pa. The deposition rate and the overall amount of Nb_2O_5 or Ta_2O_5 deposited were monitored in situ by a quartz microbalance. An amount of Nb_2O_5 and Ta_2O_5 equivalent to a nominal thickness of 100 nm was deposited for all samples. The nominal deposition rate was typically 0.03 nm/s. A complete deposition/reaction experiment required about 55 min. The substrate temperature was varied from 500 to 1100 °C, determined by a Pt/PtRh10 thermocouple. After deposition the samples were kept in the chamber and cooling down to room temperature while the oxygen partial pressure was held to avoid an additional oxygen deficiency.

The phases present in the samples after the reaction, and their orientation relationships, were investigated by X-ray diffraction (XRD) (Philips X'pert MRD) with Cu Kα radiation. The 2θ angle was scanned at a speed of 0.18°/min, and pole figures were taken with 2° steps of the ψ value.

Specimen preparation for (high-resolution) transmission electron microscopy, (HR)TEM, was straightforward using the standard grinding and ion milling tools. The final ion milling step was performed in a Gatan DuoMill at 3 kV, and at an incidence angle of 13–14°. The TEM observations were carried out in a Philips CM20 operated at 200 kV and a JEOL 4010 operated at 400 kV. For the JEOL 4010, a spherical aberration of 1 nm, a defocus spread of 8.0 nm, and a beam semi-convergence angle of 0.7 mrad were characteristic. HRTEM images were recorded by either negatives or a digital CCD camera. HRTEM negatives were then digitized by scanning (2048 × 2048 pixels) and the gray scale was adapted to achieve reasonable contrast.

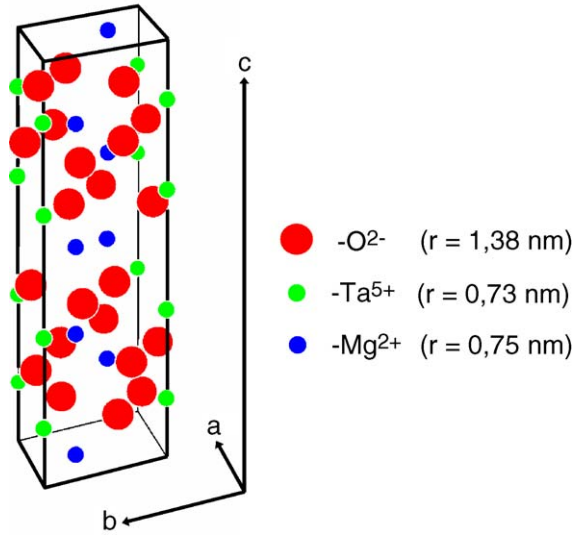

Fig. 1. Crystal structure of $Mg_4Ta_2O_9$.[9]

3. Results and discussion

3.1. X-ray diffraction

Mainly two product phases were found in each of the two systems $MgO–Nb_2O_5$ and $MgO–Ta_2O_5$, viz. $Mg_4Nb_2O_9$ and $MgNb_2O_6$, and $Mg_4Ta_2O_9$ and $MgTa_2O_6$ phases, respectively. In this paper, we concentrate on $Mg_4Nb_2O_9$ and $Mg_4Ta_2O_9$. Details on phase formation and on the $MgNb_2O_6$ and $MgTa_2O_6$ phases have been published elsewhere.[27,28] $Mg_4Nb_2O_9$ and $Mg_4Ta_2O_9$ are both hexagonal (space group $P\bar{3}c1$, No. 165) with the lattice parameters $a = b = 0.51624$ nm and $c = 1.4024$ nm for $Mg_4Nb_2O_9$ [JCPDS 38-1459], and $a = b = 0.51611$ nm and $c = 1.40435$ nm for $Mg_4Ta_2O_9$ [JCPDS 38–1458].

Fig. 1 shows the crystal structure of $Mg_4Ta_2O_9$.[9] It has a distorted hexagonal close packed stacking of oxygen ions along the c axis. It is isotypic with the corundum-type (α-Al_2O_3) structure, with cations occupying two thirds of the octahedral interstices of the oxygen frame. The structure of $Mg_4Nb_2O_9$[16,17] is quite similar to that of $Mg_4Ta_2O_9$, with a very small difference in the lattice parameters. Due to this fact the results obtained on $Mg_4Nb_2O_9$ and $Mg_4Ta_2O_9$ were most similar to each other. Thus the obtained results are presented in this paper on the example of either the one or the other of the two materials.

The formation of $Mg_4Nb_2O_9$ and $Mg_4Ta_2O_9$ phases was systematically investigated by XRD as a function of temperature. Table 1 shows the orientation relationships at different temperatures and the misfit values observed for these two phases. Fig. 2 shows typical pole figures taken at $2\theta = 19.8°$ corresponding to $Mg_4Ta_2O_9$ (1 0 .0)[1] for samples prepared at 800,

[1] In this paper, the hexagonal three-index system is used, the dot indicating the omitted fourth index.[29,30]

Table 1
Tantalate and niobate orientation dependence on temperature and $Mg_4(Nb,Ta)_2O_9$/MgO misfit

Phases	Temperature range (°C)	Parallel planes	Parallel direction	NCSL misfit $\delta1//[\bar{1}\,1\,0]_{MgO}$ (%)	NCSL misfit $\delta2//[\bar{1}\,1\,0]_{MgO}$ (%)
$Mg_4Ta_2O_9$	700–1100	$(1\,1\,.4)//(0\,0\,1)_{MgO}$	$[1\,\bar{1}\,.0]//[1\,\bar{1}\,0]_{MgO}$	6.4	
	850–1000	$(1\,1\,.6)//(0\,0\,1)_{MgO}$	$[1\,\bar{1}\,.0]//[1\,\bar{1}\,0]_{MgO}$	−4.2	0.1
	950–1000	$(1\,1\,.9)//(0\,0\,1)_{MgO}$	$[1\,\bar{1}\,.0]//[1\,\bar{1}\,0]_{MgO}$	9.4	
$Mg_4Nb_2O_9$	700–1100	$(1\,1\,.4)//(0\,0\,1)_{MgO}$	$[1\,\bar{1}\,.0]//[1\,\bar{1}\,0]_{MgO}$	6.3	
	900–1000	$(1\,1\,.6)//(0\,0\,1)_{MgO}$	$[1\,\bar{1}\,.0]//[1\,\bar{1}\,0]_{MgO}$	−4.3	0.2
	1000	$(1\,1\,.9)//(0\,0\,1)_{MgO}$	$[1\,\bar{1}\,.0]//[1\,\bar{1}\,0]_{MgO}$	9.3	

900 and 1000 °C, respectively. The pole figures are plotted with the pole angle $\psi = 0°$ at the center and with the rim corresponding to $\psi = 90°$. ($\psi = 90°$ corresponds to the substrate surface being parallel to the plane defined by incident and reflected X-ray beams.) Fig. 2(a) shows that at 800 °C, only the peaks at $\psi = 45°$ are present. This is due to the orientation relationship $Mg_4Ta_2O_9$ (1 1 .4)//MgO (0 0 1), because of the angle $\angle Mg_4Ta_2O_9$ (1 0 .0);(1 1 .4) = 45.8°. In Fig. 2(b) for a sample made at 900 °C, in addition to the peaks at $\psi = 45°$, there are peaks at $\psi = 54°$ which are from the orientation relationship $Mg_4Ta_2O_9$ (1 1 .6)//MgO (0 0 1) (cf. $\angle Mg_4Ta_2O_9$ (1 0 .0);(1 1 .6) = 54.4°). Each peak at $\psi = 54°$ is split into two sub-peaks with an interval of $\Delta\phi = 14°$. In Fig. 2(c) for a sample made at 1000 °C, the newly observed peaks at $\psi = 63°$ are arising from the orientation relationship $Mg_4Ta_2O_9$ (1 1 .9)//MgO (0 0 1) (cf. $\angle Mg_4Ta_2O_9$ (1 0 .0);(1 1 .9) = 63.4°). Each of them are split into two sub-peaks with an interval of $\Delta\phi = 22°$. From a series of pole figures and ϕ scans, the in-plane orientation is found to be $Mg_4Ta_2O_9$ [1 $\bar{1}$ .0]//MgO [1 $\bar{1}$ 0] for all the orientations observed. For the Nb_2O_5–MgO system, the same three orientation relationships were found.

From the three orientations one may generalize that the primary motif of the topotaxial reaction for the two phases is governed by the relation $Mg_4(Nb/Ta)_2O_9$ [1 $\bar{1}$ .0]//MgO [1 $\bar{1}$ 0]. The (1 1 .4) orientation has been reported before by Manabe et al.[18], while the other two orientations seem to be new findings. The orientation relationship (1 1 .6) deviates from the (1 1 .4) one by a rotation of 11.4° around the $Mg_4(Nb/Ta)_2O_9$ [1 $\bar{1}$ .0]/MgO [1 $\bar{1}$ 0] common axis, while the orientation relationship (1 1 .9) deviates from the (1 1 .4) one by a rotation of 22.5° around this axis.

3.2. SAED and HRTEM

To evaluate the three orientations on a microstructural scale, we employed TEM (and HRTEM), and studied selected area electron diffraction (SAED) patterns. The latter fully confirmed the XRD results.

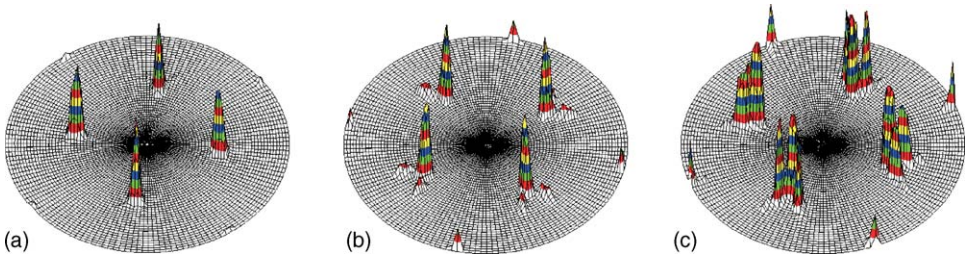

Fig. 2. Pole figures at $2\theta = 19.8°$, corresponding to $Mg_4Ta_2O_9$ (1 0 .0), for samples made at three different temperatures: (a) 800 °C, (b) 900 °C, (c) 1000 °C. Peaks situated at $\psi = 45$, 54 and 63° are from (1 1 .4), (1 1 .6) and (1 1 .9) orientations, respectively.

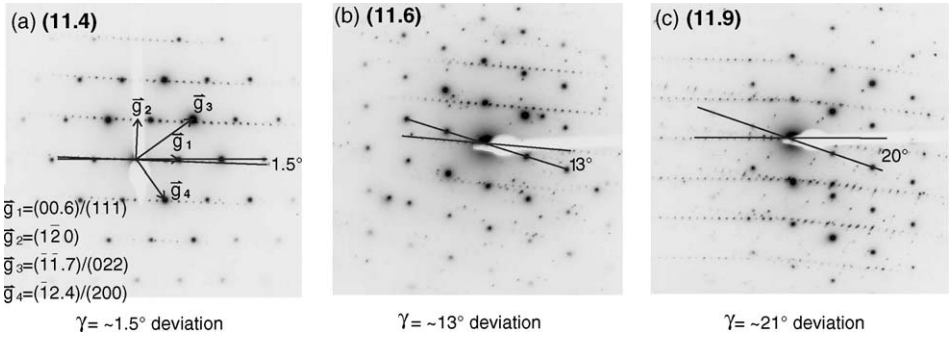

Fig. 3. SAED patterns in $Mg_4Ta_2O_9$ [2 1 .0] incidence from three grains with different orientations: (a) $Mg_4Ta_2O_9$ (1 1 .4)//MgO (0 0 1), (b) $Mg_4Ta_2O_9$ (1 1 .6)//MgO (0 0 1), and (c) $Mg_4Ta_2O_9$ (1 1 .9)//MgO (0 0 1). The narrow spaced lines of reflections represent the $Mg_4Ta_2O_9$ {0 0 .l} family. The angle γ between $Mg_4Ta_2O_9$ (0 0 .1) and MgO (1 1 1) is about 1.5, 13 and 21° in (a), (b) and (c), respectively.

Fig. 3 shows $Mg_4Ta_2O_9$ diffraction patterns from three grains with different orientation relationships. The beam direction is $Mg_4Ta_2O_9$ [2 1 .0] ⊥ [0 0 .1]. In Fig. 3(a), the basal vectors $\vec{g}_1$ and $\vec{g}_2$ are (0 0 .6) and (1 $\bar{2}$ .0) of $Mg_4Ta_2O_9$, respectively. Along the inserted line, there are six $Mg_4Ta_2O_9$ spots in between two strong MgO {1 1 1} spots, which indicates that one $Mg_4Ta_2O_9$ (0 0 .6) plane matches one MgO (1 1 1) plane in real space. As the analysis shows, the grain has the orientation $Mg_4Ta_2O_9$ (1 1 .4)//MgO (0 0 1). Defining the angle γ as ∠$Mg_4Ta_2O_9$ (0 0 .1);MgO (1 1 1), we can deduce from Fig. 3(a) that $\gamma \approx 1.5^\circ$.

Fig. 3(b) is a diffraction pattern of a grain with the orientation $Mg_4Ta_2O_9$ (1 1 .6)//MgO (0 0 1), showing that $\gamma \approx 13^\circ$, and in Fig. 3(c), taken from a grain with the orientation $Mg_4Ta_2O_9$ (1 1 .9)//MgO (0 0 1), $\gamma \approx 21^\circ$. Obviously, the experimentally determined angles $\gamma \approx 13^\circ$ and $\gamma \approx 21^\circ$ well correspond to the calculated ones, viz. ∠$Mg_4Ta_2O_9$ (1 1 .4);(1 1 .6) = 11.4° and ∠$Mg_4Ta_2O_9$ (1 1 .4);(1 1 .9) = 22.5°, respectively.

Fig. 4 schematically summarizes the orientation relationships as determined from SAED. (Although shown for $Mg_4Ta_2O_9$, this figure is equally well valid for $Mg_4Nb_2O_9$.) Fig. 4(a) and (b) show the orientation relationship $Mg_4Ta_2O_9$ (1 1 .4)//MgO (0 0 1). The viewing direction is $Mg_4Ta_2O_9$ [2 2 .$\bar{1}$]//Mg [1 1 0] in Fig. 4(a); two $Mg_4Ta_2O_9$ (1 $\bar{1}$ .0) planes meet three MgO ($\bar{1}$ 1 .0) planes, the latter two being parallel to each other. They include a NCSL misfit of $2\{(2d_{(1\,\bar{1}\,.0)} - 3d_{\mathrm{MgO}\,(\bar{1}\,1\,0)})/(3d_{\mathrm{MgO}\,(\bar{1}\,1\,0)} + 2d_{(1\,\bar{1}\,.0)})\} = 0.2\%$, cf. Table 1. In

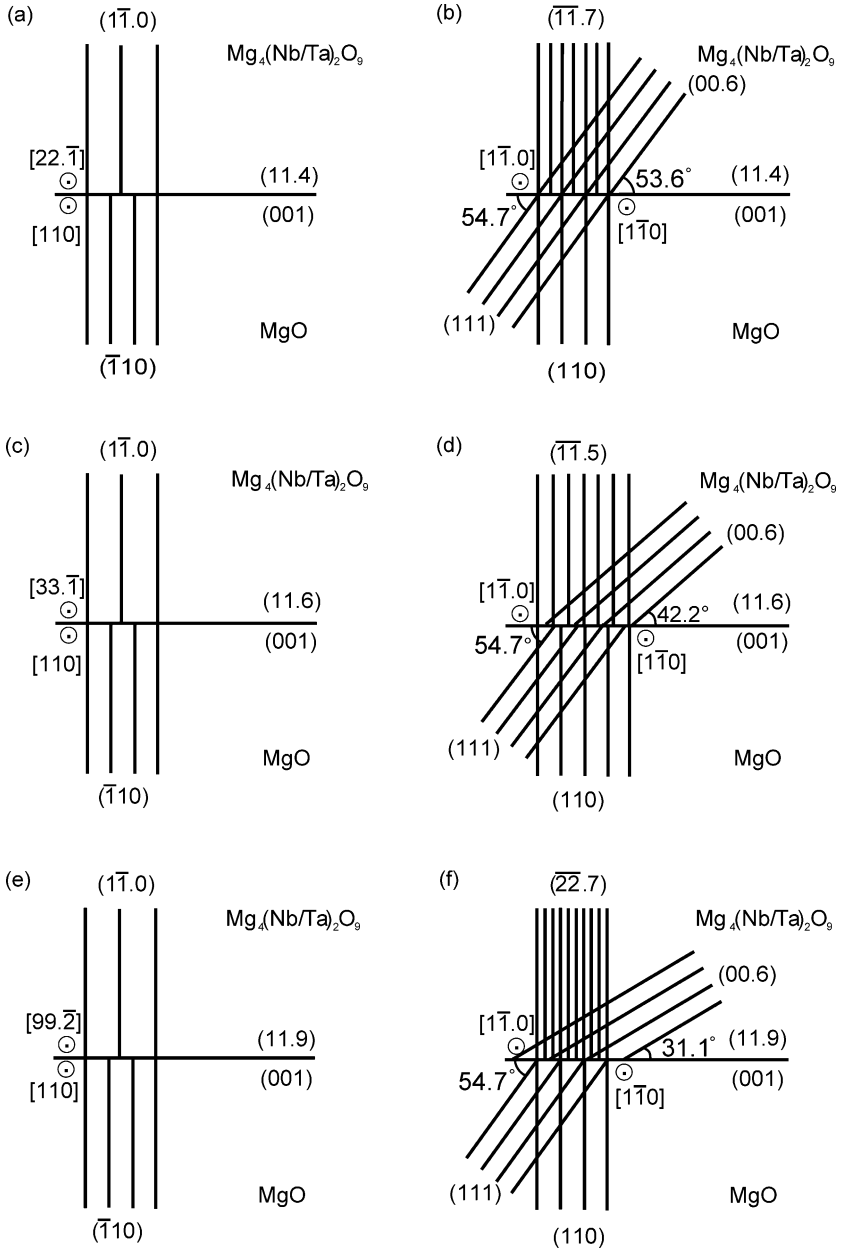

Fig. 4. Schematic illustrations of the lattice plane projections for the three orientation relationships of the $Mg_4(Nb/Ta)_2O_9$ phase on MgO: (a and b) (1 1 .4) orientation; (c and d) (1 1 .6) orientation; (e and f) (1 1 .9) orientation. Viewing directions: (a) $Mg_4(Nb/Ta)_2O_9$ [2 2 .$\bar{1}$]//Mg [1 1 0]; (b) common [1 $\bar{1}$ .0] axis, $\gamma = 1.1^\circ$; (c) $Mg_4(Nb/Ta)_2O_9$ [3 3 .$\bar{1}$]//Mg [1 1 0]; (d) common [1 $\bar{1}$ .0] axis, $\gamma = 12.5^\circ$; (e) $Mg_4(Nb/Ta)_2O_9$ [9 9 .$\bar{2}$]//Mg [1 1 0]; (f) common [1 $\bar{1}$ .0] axis, $\gamma = 23.6^\circ$.

Fig. 4(b), the viewing direction is the common $Mg_4Ta_2O_9$ [1 $\bar{1}$ .0]//MgO [1 $\bar{1}$ 0] axis. Two $Mg_4Ta_2O_9$ ($\bar{1}$ $\bar{1}$ .7) planes meet one MgO (1 $\bar{1}$ .0) plane, including a misfit of $2\{(2d_{(\bar{1}\,\bar{1}\,.7)} - d_{MgO\,(1\,1\,0)})/(d_{MgO\,(1\,1\,.0)} + 2d_{(\bar{1}\,\bar{1}\,.7)})\} = 6.4\%$. The $Mg_4Ta_2O_9$ (0 0 .6) planes meet the close-packed MgO (1 1 1) planes at a small angle of 1.1°.

Fig. 4(c) and (d) show the situation for the orientation relationship $Mg_4Ta_2O_9$ (1 1 .6)//MgO (0 0 1). The viewing direction is $Mg_4Ta_2O_9$ [3 3 .$\bar{1}$]//Mg [1 1 0] in Fig. 4(c). In Fig. 4(d), three $Mg_4Ta_2O_9$ ($\bar{1}$ $\bar{1}$ .5) planes meet two MgO (1 $\bar{1}$ .0) planes, including a misfit of $(3d_{(\bar{1}\,\bar{1}\,.5)} - 2d_{MgO\,(1\,1\,0)})/2d_{MgO\,(1\,1\,0)} = -4.2\%$. Compared to Fig. 4(b), the $Mg_4Ta_2O_9$ (0 0 .6) plane is rotated around the common [1 $\bar{1}$ .0] axis by 12.5°.

Fig. 4(e) and (f) show the situation for the orientation $Mg_4Ta_2O_9$ (1 1 .9)//MgO (0 0 1). The viewing direction is $Mg_4Ta_2O_9$ [9 9 .$\bar{2}$]//Mg [1 1 0] in Fig. 4(e). In Fig. 4(f) three $Mg_4Ta_2O_9$ ($\bar{2}$ $\bar{2}$ .7) planes meet one MgO (1 1 0) plane, including a misfit of $2\{(3d_{(\bar{2}\,\bar{2}\,.7)} - d_{MgO\,(1\,1\,0)})/(d_{MgO\,(1\,1\,0)} + 3d_{(\bar{2}\,\bar{2}\,.7)})\} = 9.4\%$. Now the $Mg_4Ta_2O_9$ (0 0 .6) planes are at an angle of 23.6° with the MgO (1 1 1) plane.

Whether and how these models indeed correspond to the situation in real space, and how they interfere with the morphology of the reaction fronts, has been investigated by HRTEM. Fig. 5 shows a HRTEM image of the $Mg_4Ta_2O_9$ (1 1 .4)/MgO (0 0 1) interface. The two inserted lines show the interplanar distance of 1.4 nm, which is the lattice parameter c of $Mg_4Ta_2O_9$. Six MgO (1 1 1) interplanar distances fit one $Mg_4Ta_2O_9$ (0 0 .1) distance. There is an angle $\gamma \approx 1.5°$ in between them, in agreement with the diffraction result of Fig. 3(a). The interface is locally rough, some periodic contrast appearing at interfacial ledges (as shown by the arrows).

Fig. 6(a) shows a HRTEM image of the (1 1 .6)/MgO (0 0 1) interface. Inserted lines define the $Mg_4Ta_2O_9$ (0 0 .1) interplanar distance of 1.4 nm, corresponding to 7d (1 1 1) MgO. The deviation angle $\gamma = 12.5°$ is indicated. The interface has a stepped morphology including plane sections. This is most probably due to the rather low misfit value here, cf. Table 1.

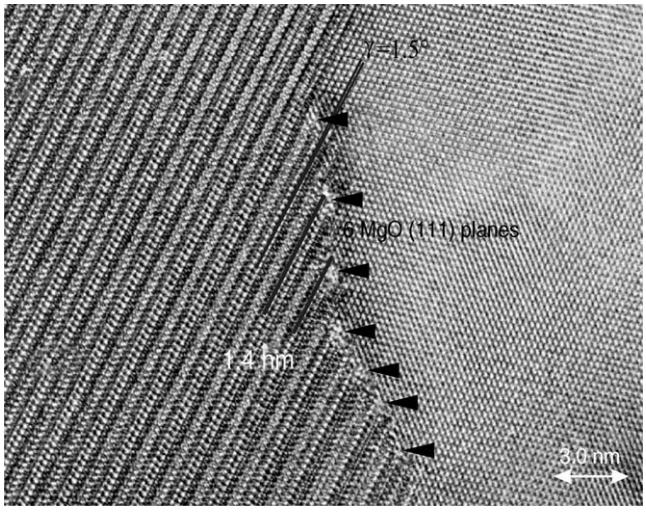

Fig. 5. HRTEM image of the interface $Mg_4Ta_2O_9$ (1 1 .4)/MgO (0 0 1). Common [1 $\bar{1}$ .0] incidence.

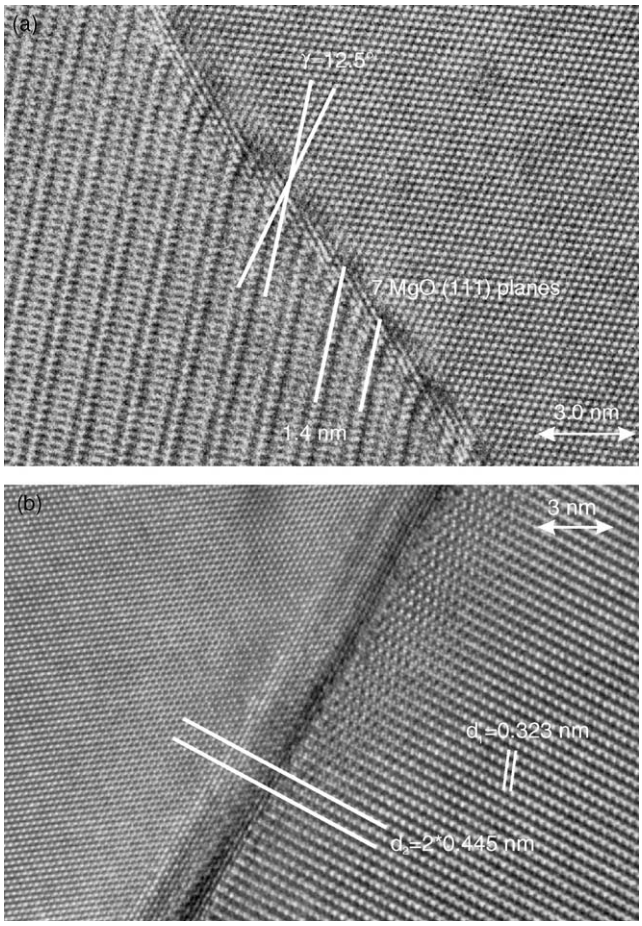

Fig. 6. HRTEM images of the interface $Mg_4Ta_2O_9$ (1 1 .6)/MgO (0 0 1): (a) common [1 $\bar{1}$ .0] incidence; (b) $Mg_4Ta_2O_9$ [3 3 .$\bar{1}$]//Mg [1 1 0] incidence.

Fig. 6(b) shows another viewing direction, viz. [3 3 .$\bar{1}$]//MgO [1 1 0]. $d_1 = 0.445$ nm corresponds to the interplanar distance of $Mg_4Ta_2O_9$ (1 $\bar{1}$ .0). Two (1 $\bar{1}$ .0) planes meet three MgO ($\bar{1}$ 1 .0) planes in real space, in accordance with Fig. 5(c). The indicated interplanar distance $d_2 = 0.323$ nm corresponds to $Mg_4Ta_2O_9$ (1 0 .3).

Fig. 7 shows the HRTEM image of the (1 1 .9)/MgO (0 0 1) interface. The 1.4 nm spacing of (0 0 .1) $Mg_4Ta_2O_9$ is seen again,

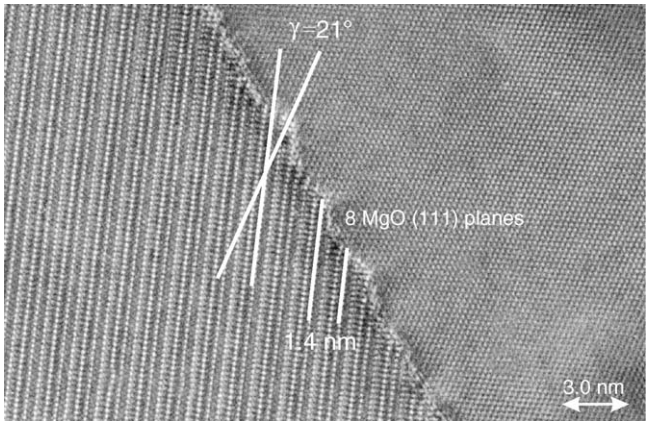

Fig. 7. HRTEM image of the interface $Mg_4Ta_2O_9$ (11.9)/MgO (0 0 1).

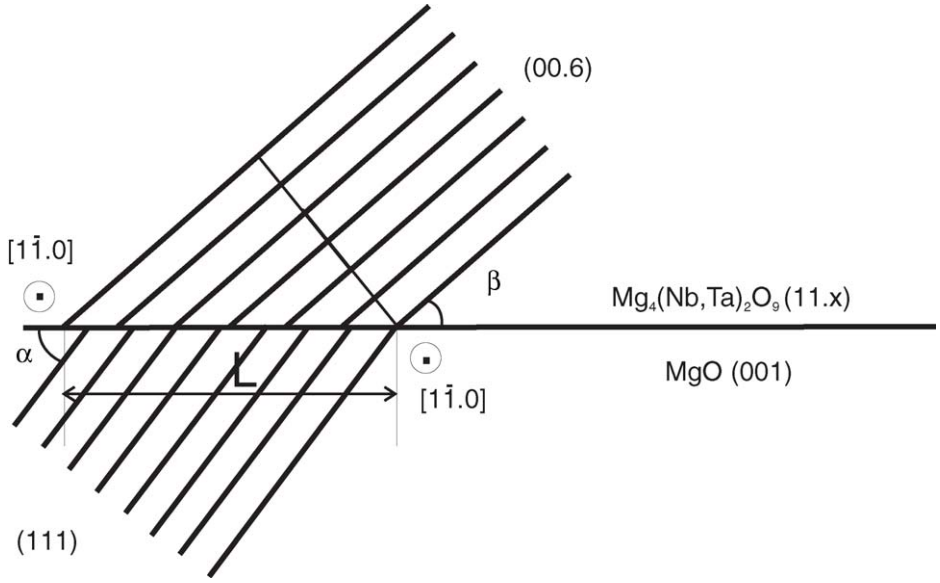

Fig. 8. Geometric model for the interface $Mg_4(Nb/Ta)_2O_9$ (1 1 .*x*)/MgO (0 0 1). *L* is the periodic repeating length of the two matched lattices at the interface.

this time corresponding to 8*d* (1 1 1) MgO. The angle γ appears to be 21°. The interface has a wavy morphology.

Figs. 5–7 clearly demonstrate that the common axis $Mg_4Ta_2O_9$ [1 $\bar{1}$ .0]//MgO [1 $\bar{1}$ 0] is observed for all three orientations, the latter differing by the angle (of 0°, ~12.5° and ~21°, respectively) included by the close packed planes of the product phase and MgO. The three orientations can be described by a common geometric model (Fig. 8). Let *L* be the periodic repeating length of the two matched lattices at the $Mg_4(Nb/Ta)_2O_9$ (1 $\bar{1}$.*x*)/MgO (0 0 1) interface. In the (1 1 .4) case, one $Mg_4(Nb/Ta)_2O_9$ (0 0 .1) interplanar distance corresponds to six MgO (1 1 1) planes. After incline, we expect more MgO (1 1 1) planes, viz. (*n* + 6) in total, to match one $Mg_4(Nb/Ta)_2O_9$ (0 0 .1) plane. From this, the following equations can be decuced:

$$L \sin\beta = d_{(0\,0\,.1)} \quad \text{and} \quad L\cos(90^\circ - \alpha) = (n+6)d_{\mathrm{MgO}\,(1\,1\,1)}.$$

We then obtain:

$$\sin\beta = \frac{\cos(90^\circ - \alpha)d_{(0\,0\,.1)}}{(6+n)d_{\mathrm{MgO}\,(1\,1\,1)}}.$$

Inserting the values $d_{(0\,0\,.1)} = 1.404$ nm, $d_{\mathrm{MgO}\,(1\,1\,1)} = 0.243$ nm, and $\alpha = 54.7°$, we obtain:

$n = 0 \quad \beta = 51.8°, \quad \gamma = \alpha - \beta = 2.9°;$

$n = 1 \quad \beta = 42.3°, \quad \gamma = \alpha - \beta = 12.4°;$

$n = 2 \quad \beta = 36.1°, \quad \gamma = \alpha - \beta = 18.6°.$

Obviously, the values *n* = 0, 1, 2 correspond to the three orientations (1 1 .4), (1 1 .6) and (1 1 .9), respectively, as can be seen from the calculated values for the angle γ. It appears that these orientations are not accidental, but rather correspond to relative minima of the lattice misfit under the condition of a common $Mg_4Ta_2O_9$ [1 $\bar{1}$ .0]//MgO [1 $\bar{1}$ 0] axis. The occurence of all three orientations is most probably a consequence of a facetted morphology of the MgO (0 0 1) surface. MgO is known to develop various stepped and facetted surfaces during annealing, depending on temperature.[19–21] Different facets may lead to different nucleation conditions and thus to differently oriented product phases, as shown in the following section.

4. A near-coindidence site lattice model and the faceting of MgO (0 0 1)

The coincidence site lattice (CSL) model has had enormous success in explaining grain boundary structures in cubic materials with whatsoever metallic, ionic or covalent bondings involved. The correlation between CSL-related misorientations and special properties is frequently striking, so that some interest has risen to extend the work from grain boundaries in cubic crystal structures to interfaces in materials of lower symmetry.[22] However, the application of these ideas is more complicated in non-cubic materials and phase boundaries, where the special conditions necessary for lattice coincidence do not generally exist. In this section, we will try to deal with the question using a cube-on-cube model based on the translation of the hexagonal into an equivalent cubic unit cell. Here, a near coincidence site lattice (NCSL) as opposed to an exact CSL is sought, allowing a mismatch in the lattices being superimposed.

Although there are different kinds and numbers of atoms in the hexagonal $Mg_4Nb_2O_9$/$Mg_4Ta_2O_9$ and cubic MgO structures, the oxygen sublattices are similar. The cations are situated at the anion octahedron interstitial positions. Thus we just consider the oxygen sublattices which represent the rigid frame of the two lattices and are responsible for the orientations during the reaction.[23]

To replace the hexagonal $Mg_4Nb_2O_9$/$Mg_4Ta_2O_9$ cell in the NCSL model, an equivalent cubic cell is constructed, considering the oxygen sublattice only. Fig. 9 schematically shows the principle. Starting from a cubic cell, an equivalent hexagonal cell is constructed, for simplicity neglecting any detailed differences between cubic and hexagonal symmetry. The obtained relations will then permit to construct an equivalent cubic cell

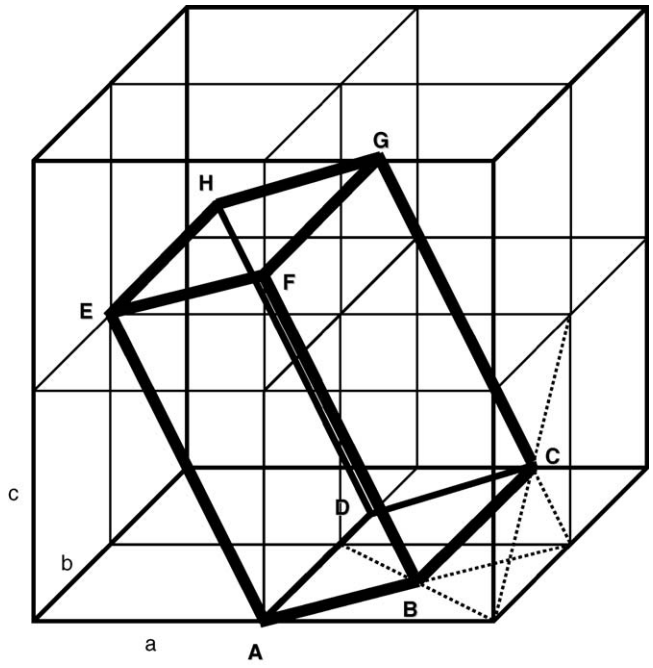

Fig. 9. Schematic representation of the relationship between a cubic lattice (thin lines) and a chosen equivalent hexagonal cell ABCDEFGH (thick lines). a, b and c are the basic vectors of the cubic cell; AB, AD and AE are the basic vectors of the constructed hexagonal cell. Dashed lines indicate the diagonals of the cubic unit cell.

to replace the original hexagonal $Mg_4Nb_2O_9/Mg_4Ta_2O_9$ cell. Fig. 9 shows eight unit cells of a cubic lattice with the lattice parameter a. The hexagonal cell highlighted by thick lines has the dimesions $\sqrt{2}/2a \times \sqrt{2}/2a \times \sqrt{3}a$, and a cell volume of $0.75a^3$. Note that the c-axis of the hexagonal cell is parallel to the body diagonal of the cubic cell, while its a-axis is parallel to the diagonal of the basal plane in the cubic cell. To balance the number of oxygen atoms between the two cells, the three axes of the hexagonal cell should be multiplied by a factor of two, resulting in a cell with a size $\sqrt{2}a \times \sqrt{2}a \times 2\sqrt{3}a$ and a volume $V_{hex} = 6V_{cubic}$. Thus the equivalent cubic cell, which should finally replace the hexagonal $Mg_4Nb_2O_9/Mg_4Ta_2O_9$ cell, has a cell volume of $V_{cubic} = V_{hex}/6$. Considering that $V_{hex} = a_{hex}^2 c_{hex} \sin 60^\circ$, a cell volume V_{hex} of 0.32367 and 0.32396 nm^3 results for $Mg_4Nb_2O_9$ and $Mg_4Ta_2O_9$, respectively. Taking $V_{hex} = 0.324$ nm^3, we obtain $V_{cubic} = 0.054$ nm, from which the lattice parameter of the equivalent cubic cell results as $a = 0.378$ nm.

Now we can analyze the orientation relationships between the hexagonal $Mg_4Nb_2O_9/Mg_4Ta_2O_9$ and the cubic MgO lattices with a simple cube-on-cube model, i.e., the pseudocubic lattice of $Mg_4Nb_2O_9/Mg_4Ta_2O_9$ on the cubic MgO one. Considering two interpenetrating crystal lattices, there exist some special misorientations which result in high densities of coincident lattice sites. Here we superimpose the $\{1\,1\,0\}$ planes of MgO and the pseudo-cubic lattice, with the common (tilt) axis being always aligned along the pseudo-cubic $[1\,\bar{1}\,0]$ direction ($Mg_4Ta_2O_9$ $[1\,\bar{1}\,.0]$)//MgO $[1\,\bar{1}\,0]$). It should be noted that unlike a usual CSL model which considers in-plane misorientations rotating around the surface normal, here we consider the misorientations rotating around an axis lying in the surface, which is equivalent to a cross section view. In the presence of a high density of steps on a substrate surface, the lattice mismatch along the surface normal should be taken into consideration, for the film has to accommodate the distortion due to the mismatch between the substrate step height and the lattice constant of the growing film.

Near-coincidence is determined by the smallness of the misfit between the different position vectors of the two superimposed lattices. Let a_{MgO} be the lattice constant of MgO and a_p be the lattice constant of the pseudo-cubic niobate/tantalate cell. Viewing along the direction $\langle 1\,1\,0\rangle$, the two rectangular lattices are $\sqrt{2}a_{MgO} \times a_{MgO}$ and $\sqrt{2}a_p \times a_p$, respectively. Let k and l be the x and y coordinates of the position vectors corresponding to lattice points in MgO, and let m and n be the corresponding coordinates in the pseudo-cubic lattice. Then $\sigma_{MgO} = 2k^2 + l^2$ is the square of the position vector $[k, l]$, and likewise $\sigma_p = 2m^2 + n^2$ is the square of the position vector $[m, n]$. The NCSL lattices are produced by rotating two crystals about their common $[1\,\bar{1}\,0]$ axes, i.e. the origin O is a common point and the points $[k, l]$ and $[m, n]$ are assumed to be coincident for a specific rotation angle of the two crystals. After superimposing the lattices, the misfit δ for various combinations of σ_{MgO} and σ_p is calculated as

$$\delta = \frac{a_{MgO}\sigma_{MgO}^{1/2} - a_p\sigma_p^{1/2}}{(a_{MgO}\sigma_{MgO}^{1/2} + a_p\sigma_p^{1/2})/2}. \quad (1)$$

For each set of the near matched σ_{MgO} and σ_p, the misorientations (relative rotations) between the $\langle 1\,1\,0\rangle$ principle axes of the two lattices were calculated by

$$\theta = \mathrm{tg}^{-1}\left(\frac{n}{\sqrt{2}m}\right) - \mathrm{tg}^{-1}\left(\frac{l}{\sqrt{2}k}\right). \quad (2)$$

The equation was calculated for all possible permutations of k, l, m and n between 0 and 7. The choice of small position vec-

Table 2
Calculated possible NCSLs for [1 1 0] rotated orientations and $\sigma_{MgO} < 100$. $a_{MgO} = 0.4211$ nm, $a_p = 0.378$ nm

k	l	m	n	σ_{MgO}	σ_p	θ (°)	δ (%)
1	0	1	0	2	2	0	10.8
2	0	2	1	8	9	19.5	4.8
2	1	2	2	9	12	15.8	−3.6
3	0	3	2	18	22	25.2	0.8
3	1	3	2	19	22	11.9	3.5
3	2	3	3	22	27	10.1	0.6
4	0	4	3	32	41	27.9	−1.6
4	1	4	3	33	41	17.9	−0.05
4	2	4	3	36	41	8.4	4.3
4	3	4	4	41	48	7.3	2.9
5	0	5	3	50	59	23.0	2.5
5	0	5	4	50	66	29.5	−3.1
6	0	6	5	72	97	30.5	−4.1
6	1	6	3	73	81	12.7	5.6
6	1	6	4	73	88	18.5	1.5
6	1	6	5	73	97	23.8	−3.4
6	2	6	5	76	97	17.2	−1.4
7	0	7	2	98	102	11.4	8.7
7	0	7	4	98	114	22.0	3.2

tors ensured that the σ values correspond to a high density of coincident lattice sites and hence to a low energy. Table 2 lists all the calculated misorientations with $\sigma_{MgO} < 100$ and $\delta < 6\%$, except for the $\theta = 0$ case with $\delta = 10.8\%$, and the $\theta = 11.4^\circ$ case with $\delta = 8.7\%$. Notably, if we consider a misorientation angle of $11.4 \pm 1.3^\circ$, we find several possible combinations of $(k, l) \sim (m, n)$, such as $(3, 1) \sim (3, 2)$, $(3, 2) \sim (3, 3)$, $(6, 1) \sim (6, 3)$ and $(7, 0) \sim (7, 2)$ resulting in such an angle. And the combinations $(k, l) \sim (m, n)$ of $(2, 0) \sim (2, 1)$, $(3, 0) \sim (3, 2)$, $(4, 1) \sim (4, 3)$, $(5, 0) \sim (5, 3)$, $(6, 1) \sim (6, 4)$, $(6, 1) \sim (6, 5)$, and $(7, 0) \sim (7, 4)$ result in a misorientation angle of $21.6 \pm 3.6^\circ$. In our experiments, we frequently observed these misorientation angles and we denoted them as (1 1 .6) and (1 1 .9), respectively. Considering the experimental error of $\pm 0.5^\circ$ and a tolerance of a deviation of $\sim 3^\circ$, we see that the calculated angles match the observed values (from both SAED patterns and the HRTEM images) very well. There might be some other misorientations for the grains present in our film, but as predicted by the calculation, the percentage is very low and the probability to find them by TEM and HRTEM is much lower compared with so far observed ones.

The cube-on-cube relationship of $\theta = 0^\circ$, i.e. the (1 1 .4) case, is most frequently observed despite the large misfit of 10.8%. Its presence can be explained by the fact that the macroscopic surface of the single crystal MgO substrate is (0 0 1), and it is not atomically flat but has steps and terraces. These surface steps and terraces favour the cube-on-cube epitaxy as the orientation is already fixed in two mutually perpendicular directions.

Fig. 10 illustrates some of the selected coincidence site lattice models. One can see that the different angles between the pseudocubic lattice and the MgO substrate correspond to different faceting modes and angles.

Fig. 11 shows a schematic illustration of a pit on the MgO (0 0 1) surface and the niobate/tantalate nucleation for three different orientations along ⟨1 1 0⟩. Around a large pit frequently seen on the MgO (0 0 1) surface, there are many positions where the tangent planes correspond to different faceting angles of the MgO (0 0 1) surface.

We investigated the substrate surface by AFM and found many steps running along MgO ⟨1 1 0⟩. We conclude that the faceting of MgO represents a constraint for all the possible pre-

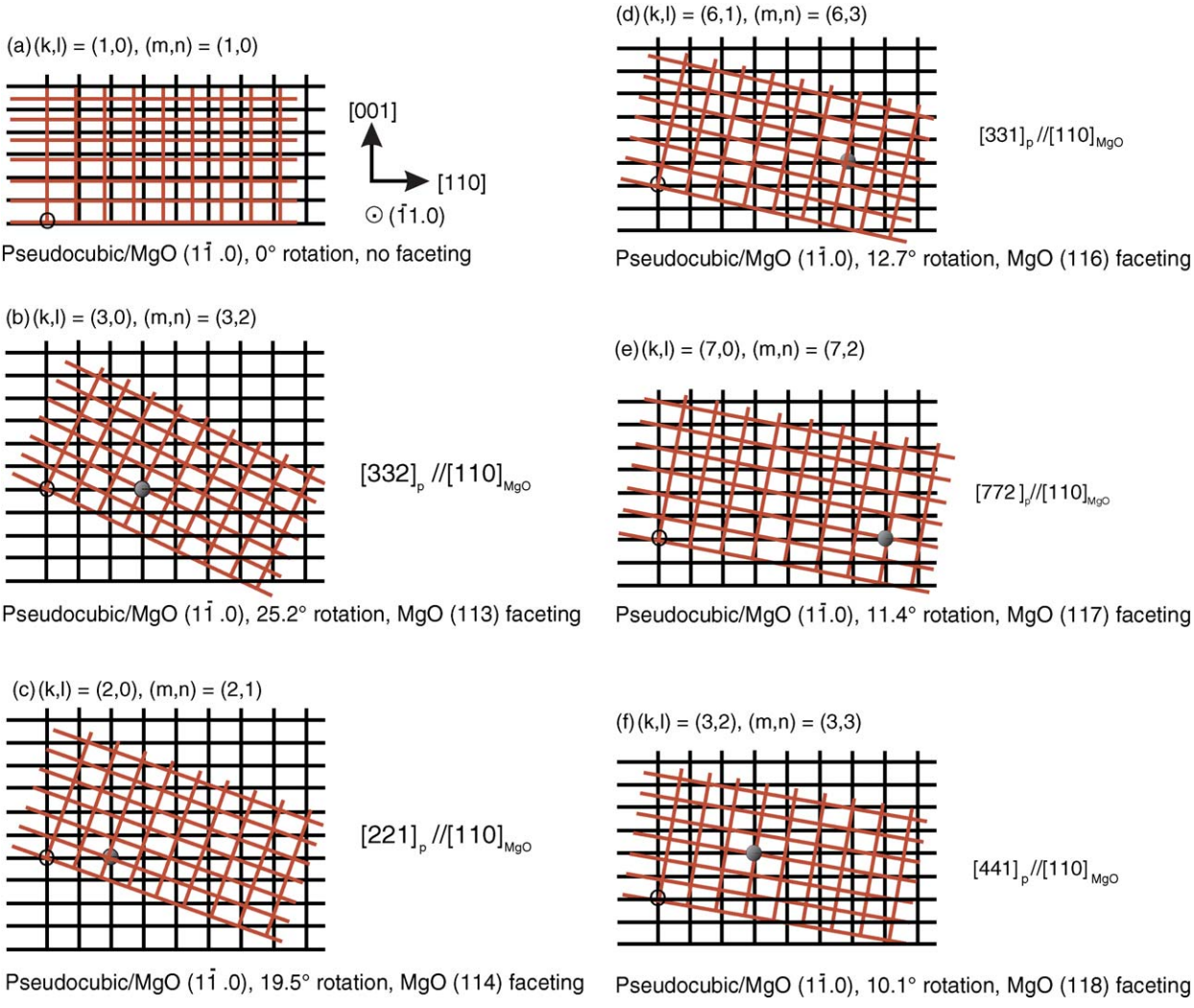

Fig. 10. Illustrations of some selected coincident site lattices and probable corresponding faceting of the substrate surface along ⟨1 1 0⟩. Note the angles 25.2, 19.4, 15.8, 13.2, 11.4 and 10.0° corresponding to (1 1 3), (1 1 4), (1 1 5), (1 1 6), (1 1 7) and (1 1 8) faceting, respectively.

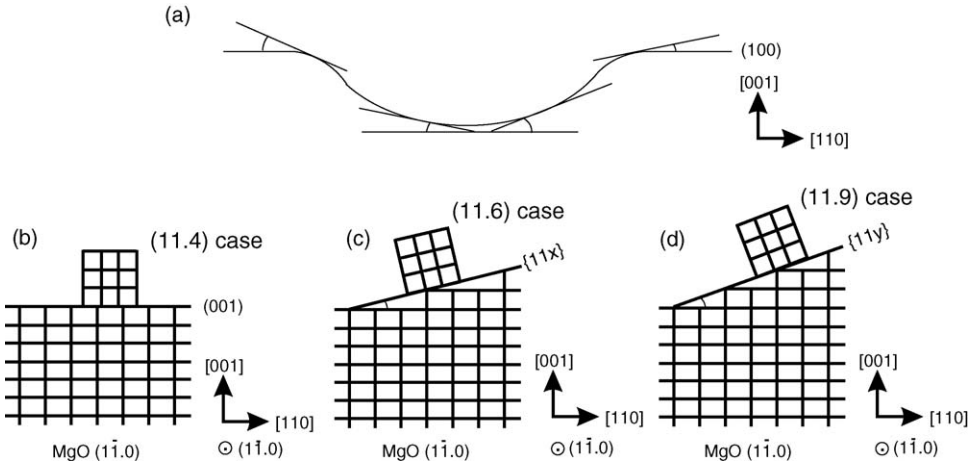

Fig. 11. Schematic illustrations of a pit on the MgO (0 0 1) surface and the nucleation for the three different orientations along ⟨1 1 0⟩. (a) A large pit frequently seen on the MgO (0 0 1) substrate; (b) MgO (0 0 1) without faceting; (c) (1 1 x) (x = 6, 7, 8) faceting of the substrate, $\alpha \sim 11.65 \pm 1.65°$; (d) (1 1 y) (y = 3, 4) faceting of the substrate, $\beta \sim 22.35 \pm 2.85°$.

ferred NCSL directions, some of them becoming more favored than others during the initial stages of nucleation. Another strong evidence to support our argument is that after changing to a new batch of MgO (0 0 1) substrates involving a flat surface without large pits and high density of steps, we did no longer observe the (1 1 .6) and (1 1 .9) orientations.

5. Discussion and conclusions

A solid state reaction requires the continuous movement of the reaction front. Different microscopic mechanisms for this movement are possible, depending on (i) the symmetry of the crystal lattices of the two phases separated by the reaction front, (ii) their mutual crystallographic orientation, (iii) the lattice mismatch, and (iv) the morphology of the reaction front. In case of a spinel/MgO front, both the spinel and MgO involve a face-centered cubic oxygen sublattice, so that the anionic sublattice of the divalent oxide can principally be taken over by the growing spinel, and the misfit at the planar spinel/MgO front can be adapted by a network of misfit dislocations.[4,5] This simple mechanism, however, was enabled by a cube-on-cube orientation relationship. Other crystal lattices, other crystallographic orientations and other interface morphologies may result in other microscopic mechanisms of interface movement.

A generally well-known mechanism occuring in precipitation or reaction processes is related to the formation and movement of steps in the interface, i.e. of interfacial ledges (ledge mechanism[24,25]). A possible combination of dislocation and ledge mechanisms is the mechanism of disconnections, which represent interfacial defects combining the characters of dislocations and ledges.[26] Although the necessary conditions for one or the other of those mechanisms to occur can certainly be discussed on the base of lattice considerations, it is difficult to predict which mechanism will occur at a certain reactive interface of non-cubic character.

The present HRTEM investigations represent a first step in evaluating the microscopic mechanisms occuring at the $Mg_4Nb_2O_9$/MgO and $Mg_4Ta_2O_9$/MgO fronts, which are of non-cubic character. The surprising presence of three different orientations of the product phase, which may originate from a faceted MgO surface, results in a variety of interface morphologies in this system. As a consequence, a number of different interfacial reaction mechanisms may occur *simultaneously*. E.g., in the case of the (1 1 .6) oriented product phase, the HRTEM results suggest a ledge mechanism (cf. Fig. 7), whereas the periodic strain contrasts along the interface in the (1 1 .4) and (1 1 .9) cases (cf. Figs. 5 and 7) suggest that a mechanism is operative that involves the movement of ledges and dislocations, respectively.

The origin of this variety of orientations and mechanisms is obviously given by the initial stage of the solid state reaction, when a faceting of the MgO (0 0 1) surface results in the growth of different orientations of $Mg_4Nb_2O_9$ and $Mg_4Ta_2O_9$, respectively, as demonstrated by a near-coincidence site lattice model.

The simultaneous presence of a number of different interfacial reaction mechanisms at the $Mg_4Nb_2O_9$/MgO and $Mg_4Ta_2O_9$/MgO reaction fronts makes the analysis of the reaction mechanisms difficult. Detailed considerations of the atom arrangements in the vicinity of the reaction front will be necessary in order to draw more definite conclusions on these mechanisms.

Acknowledgement

This work was supported by DFG via SFB 418 at Martin-Luther-Universität Halle-Wittenberg.

References

1. Schmalzried, H., *Solid State Reactions*. Verlag Chemie, Weinheim, 1981.
2. Schmalzried, H., *Chemical Kinetics in Solids*. VCH-Verlag, Weinheim, 1995.
3. Boldyrev, V. V., ed., *Reactivity of Solids: Past, Present and Future*. Blackwell Science, Oxford, 1996.
4. Sieber, H., Hesse, D. and Werner, P., Misfit accommodation mechanisms at moving reaction fronts during topotaxial spinel-forming thin-film solid-state reactions: a high-resolution transmission electron microscopy study of five spinels of different misfits. *Phil. Mag. A*, 1997, **75**, 889–908.

5. Hesse, D., The submicroscopic structure of reaction fronts in solid-solid reactions and its correlation with reaction mechanism and kinetics. *Solid State Ionics*, 1997, **95**, 1–15.
6. Hesse, D., Graff, A., Senz, S. and Zakharov, N., The structure of Mg_2SnO_4/MgO topotaxial reaction fronts during gas–solid and solid–solid reactions. *Ceram. Int.*, 2000, **26**, 753–756.
7. Abbattista, F., Rolando, P. and Borroni, G., On system MgO–Nb_2O_5. *Ann. Chim. (Rome)*, 1970, **60**, 426–435.
8. Norin, R., Arbin, C. and Nolander, B., Note on phase composition of MgO–Nb_2O_5 system. *Acta Chem. Scand.*, 1972, **26**, 3389–3390.
9. Baskin, Y. and Schell, D. C., Phase studies in the binary system MgO–Ta_2O_5. *J. Am. Ceram. Soc.*, 1963, **46**, 174.
10. Kasper, H., Die Tripseudobrookitphasen $Mg_5Nb_4O_{15}$ und $Mg_5Ta_4O_{15}$, ein neuer Strukturtypus, und die Lichtabsorption von Co^{2+}, Ni^{2+} und Cu^{2+} im Pseudobrookit- und Tripseudobrookitgitter. *Z. Anorg. Allg. Chem.*, 1967, **354**, 208–224.
11. You, Y. C., Park, N., Jung, K. H., Park, H. L., Kim, K. C., Mho, S. I. *et al.*, Luminescence of cerium doped $Mg_4Nb_2O_9$ phosphor. *J. Mater. Sci. Lett.*, 1994, **13**, 1682–1683.
12. Bruck, E., Route, R. K., Raymakers, R. J. and Feigelson, R. S., Crystal growth of compounds in the MgO–Nb_2O_5 binary system. *J. Crystal Growth*, 1993, **128**, 842–845.
13. Groen, H. B., Kooi, B. J., Vellinga, W. P. and De Hosson, J. T. M., High-resolution transmission electron microscopy imaging of misfit-dislocation networks at Cu–MgO and Cu–MnO interfaces. *Phil. Mag. A*, 1999, **79**, 2083–2101.
14. Lewis, M. H., Daniel, A. M., Chamberlain, A., Pharaoh, M. W. and Cain, M. G., Microstructure-property relationships in silicate-matrix composites. *J. Microsc.*, 1993, **169**, 109–118.
15. Hesse, D. and Senz, S., Structure and chemistry of reactive interfaces in ceramics. In *Proceedings of the 10th International Ceramics Congress*, ed. P. Vincenzini, 2003, pp. 133–144, Part A.
16. Bertaut, E. F., Corliss, L., Forrat, F., Aleonard, R. and Pauthenet, R., Etude de niobates et tantalates de metaux de transition bivalents. *J. Phys. Chem. Solids*, 1961, **21**, 234–251.
17. Kumada, N., Taki, K. and Kinomura, N., Single crystal structure refinement of a magnesium niobium oxide: $Mg_4Nb_2O_9$. *Mater. Res. Bull.*, 2002, **35**, 1017–1021.
18. Manabe, T., Yamaguchi, I., Kondo, W., Mizuta, S. and Kumagai, T., Topotaxy of corundum-type tetramagnesium diniobate and ditantalate layers on rock-salt-type magnesium oxide substrates. *J. Am. Ceram. Soc.*, 1999, **82**, 2061–2065.
19. Norton, M. G., Summerfelt, S. R. and Carter, C. B., Surface preparation for the heteroepitactic growth of ceramic thin films. *Appl. Phys. Lett.*, 1990, **56**, 2246–2248.
20. Moeckly, B. H., Russek, S. E., Lathrop, D. K., Buhrman, R. A., Li, J. and Mayer, J. W., Growth of $YBa_2Cu_3O_7$ thin films on MgO: The effect of substrate preparation. *Appl. Phys. Lett.*, 1990, **57**, 1687–1689.
21. Goniakowski, J. and Noguera, C., Atomic and electronic structure of steps and kinks on MgO (1 0 0) and MgO (1 1 0). *Surf. Sci.*, 1995, **340**, 191–204.
22. King, A. H. and Singh, A., Generalizing the coincidence site lattice model to non-cubic materials. *J. Phys. Chem. Solids*, 1994, **55**, 1023–1033.
23. Carter, R. E., Mechanism of solid-state reaction between magnesium oxide and aluminum oxide and between magnesium oxide and ferric oxide. *J. Am. Ceram. Soc.*, 1961, **44**, 116–120.
24. Howe, J. M., Dahmen, U. and Gronsky, R., Atomic mechanisms of precipitate plate growth. *Phil. Mag. A*, 1987, **56**, 31–61.
25. Howe, J. M. and Benson, W. E., Determination of the atomic structure, mechanisms and kinetics of precipitate growth in solids by in situ hot-stage high-resolution transmission electron microscopy. *Interface Sci.*, 1995, **2**, 347–363.
26. Hirth, J. P. and Pond, R. C., Steps, dislocations and disconnections as interface defects relating to structure and phase transformations. *Acta Mater.*, 1996, **44**, 4749–4763.
27. Sun, D. C., Senz, S. and Hesse, D., Topotaxial formation of $Mg_4Nb_2O_9$ and $MgNb_2O_6$ thin films on MgO(0 0 1) single crystals by vapor-solid reaction. *J. Am. Ceram. Soc.*, 2003, **86**, 1049–1051.
28. Sun, D. C., Senz, S. and Hesse, D., Topotaxial formation of $Mg_4Ta_2O_9$ and $MgTa_2O_6$ thin films by vapour-solid reactions on MgO (0 0 1) crystals. *J. Eur. Ceram. Soc.*, 2004, **24**, 2453–2463.
29. Buerger, M. J., *Contemporary Crystallography*. McGraw-Hill, New York, 1970, Chapter 2.
30. Kleber, W., *An Introduction to Crystallography*. Verlag Technik, Berlin, 1970, Chapter 1.6.4.